Thermal analysis of the SMOG-1 PocketQube satellite

Róbert Kovács[a,b], Viktor Józsa[a,*]

[a] Department of Energy Engineering, Faculty of Mechanical Engineering, Budapest University of Technology and Economics, H-1111 Budapest, Műegyetem rkp. 3., Hungary
[b] Department of Theoretical Physics, Wigner Research Centre for Physics, H-1121 Budapest, Konkoly-Thege Miklós út 29-33., Hungary

HIGHLIGHTS

- Thermal analysis of the SMOG-1 picosatellite is presented.
- Results of a simple thermal network and finite element methods were compared.
- The sensitive battery just fulfills all the requirements for continuous operation.
- The thermal network model underpredicts the temperature due to its simplicity.
- A simple thermal network is able to predict the temperature variations appropriately.

ARTICLE INFO

ABSTRACT

CubeSats have revolutionized the space industry in the past two decades. Its successor, the PocketQube class seems to be a lower size limit for a satellite which can operate continuously and can be received by radio amateur equipment. The present paper discusses the simulation of the thermal environment of the SMOG-1 PocketQube satellite at low Earth orbit by both thermal network and finite element models. The major findings of the analyses are the following. Even a single node per printed circuit board model can provide adequate information about the thermal behavior without tuning the physical parameters. By applying a finite element model with few magnitudes more nodes, the predicted inner temperature increased as the losses were reduced in the radiation-dominant environment compared to the thermal network model. Therefore, this latter method provides a more conservative temperature estimation. The most sensitive component of small-sized satellites is the battery which remains in the desired positive temperature regime even in this satellite class according to the finite element model. However, the thermal network model predicted a restricted battery charging protocol to ~50% of the lit duration. Nevertheless, this condition still results in a positive energy balance by a factor of 1.5.

1. Introduction

A new era has started in space industry with the introduction of CubeSats in 1999 [1]. The $10 \times 10 \times 10$ cm satellite design (1U) brought outstanding attention since it is characterized by low development time and launch cost [2], also reviewed by NASA [3]. Such a small satellite is an excellent platform for low-cost experiments or measurements. An even smaller variant, a $5 \times 5 \times 5$ cm (1P) satellite size was proposed in 2009 by Bob Twiggs, called PocketQube, to cut further the costs and development time [4]. However, after the great success of the CubeSats, only a few groups wanted to adopt the new size. To date, there are more than fifteen known PocketQubes are under development, according to the topical web pages and the PocketQube Workshop, organized by Delfi Space. Up to now, only four PocketQubes were launched from which only the WREN satellite was 1P in size; the

others were 1.5P and 2.5P [5]. These satellites were released by the UniSat-5 mother satellite. Due to the low interest, the PocketQube specification was removed from the internet. A reason was that it was impossible to substitute eight 1P units with a 1U in a CubeSat launch pod which became a widespread standard over the years. However, the PocketQube seems to be the smallest satellite class which can operate continuously and be detected by low-cost radio amateur equipment.

The SMOG-1 PocketQube-class satellite, shown in Fig. 1, is currently being developed at the Budapest University of Technology and Economics by students and professors. This spacecraft is planned to be the successor of the MaSat-1, the first Hungarian satellite. Its principal mission is the measurement of electrosmog emitted by the land-based digital TV stations in the 430–860 MHz band [6–8], being the name-giver of the satellite. The secondary payload is a total dosimeter [9]. A Sun Synchronous Orbit (SSO) at not higher than 600 km altitude and
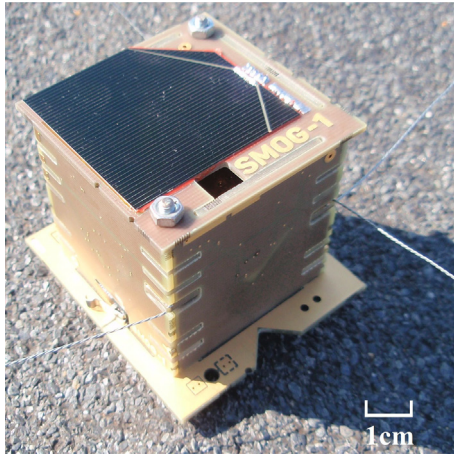
Fig. 1. The assembled satellite model for qualification tests.

Table 1
Estimated mass and average heat capacities of the main parts.

Panel	m [g]	$\bar{c}$ [J/kg K]	Role
Top	14.4	869	Solar cells with Maximum Power Point Tracking
Bottom	19.0	877	
Left	13.3	862	
Right	13.3	862	
Front	14.4	850	
Back	13.4	861	
CAP	14.8	798	Capacitor bank and connection of side panels
OBC	8.4	882	Onboard computer
COM	34.6	799	Communication and signal analysis
PCU	10.5	839	Power control unit
EPS	11.8	827	Electrical power system and dosimeter
BAT	17.2	1200	Li-Ion battery
TH	7.9	450	Threaded rod and nuts

inclination of 98° is desired to ensure an acceptably low orbit life since common commercial electronic parts are used principally to keep the project expenses low and avoid being space debris for a long time. Note that the satellite has doubled circuits which can handle a single point of failure while it runs on only one battery. The lowest acceptable altitude for the project is 400 km which ensures at least three months lifetime before re-entry to perform all the planned measurements. Currently, the estimated launch time is Q4 2019 at a 550 km SSO by the Falcon 9 launch platform. The satellite is scheduled to have a double launch since it will be carried by the UniSat-7, developed by GAUSS Srl. However, all of the satellite components and software are developed in the university, the present paper is confined to the thermal analysis. All the documentation are planned to be publicly available upon successful launch, in accordance with the pursuit of Scholz and Juang [10].

Predicting the thermal behavior of small-sized satellites is crucial since there is insufficient room for their thermal control which is often desired in the space industry [11–13]. The goal of the present paper is similar to the ones of Bulut and Sozbir [4], Corpino et al. [11], and Anh et al. [14], namely, performing thermal analysis of a small-sized satellite. However, the mentioned papers evaluate the thermal characteristics of CubeSats which have considerably larger heat capacity and internal volume than that of PocketQubes. Therefore, 1P units require a different conceptual design [5,15–19]. For further differences originated from the satellite size, see [20,21].

The novelty of the present paper is to enrich the thin literature of the thermal design of small-sized satellites. Since a detailed thermal analysis is absent in the 1P size, this work might give an insight to fellow small-size satellite developers. A thermal network (TN) model in MATLAB® Simulink® and a Finite Element Method (FEM) analysis in ANSYS® Workbench environment were established, and their results were compared. After a successful launch, the thermal behavior will be published along with the validation of the below-discussed models.

2. Materials and methods

The reason behind performing the calculations by TN and FEM is that TN is usually not computationally intensive, allowing long-term simulations to run on a single PC. The FEM model helps in setting the appropriate thermal resistances of the TN model besides revealing the detailed temperature field. The present section begins with the introduction of the satellite structure which is followed by a summary of the thermal environment. Finally, the details of the TN and FEM models are discussed.

2.1. Structure

The satellite has five internal Printed Circuit Boards (PCBs) and six side PCBs equipped with solar cells. Table 1 summarizes the mass (m) and the averaged specific heat (c) of each panel, including all electric components. The regulated voltage of the system is 3.3 V. Since selected electronic components were used in the PCBs, the efficiency of them was maximized to achieve minimal losses. The dominant power consumer is the communication and spectrum analyzer integrated circuit which dissipates 30 mA during measurement and 100 mA during transmission. A normal operating cycle consists of 9 s measurement followed by 1 s status report. This transmission begins with a Morse code for radio amateurs which is followed by a binary code of basic information about the condition of the satellite. If it passes over a trusted ground station, it might be commanded to transmit all measurement data back to Earth to clear its internal memory. Such an operation can extend up to 6 min, depending on the orbit. The concept here was to sacrifice transmission bandwidth to maximize the signal-to-noise ratio as there is very low available power on board.

The mass of the assembled satellite is 200 g, and its overall heat capacity is 171.5 J/K. Due to the low available volume (1/8 l), there is no room for a separate frame which hosts the PCBs. Therefore, these panels must serve as load carriers. However, the satellite size forces such a design choice, the structure can survive the launch procedure, proven by the desired shock tests included in the Falcon 9 User's Guide.

2.2. Thermal environment

The mean lit surface of the orbiting satellite is governed by the angular velocity. It is convenient to handle the angular velocity in a spherical coordinate system, allowing the separation of the direction vector from the magnitude. The latter affects the Maximum Power Point Tracking (MPPT) logic of the side PCBs and does not affect the mean lit surface. By neglecting the magnitude, it is assumed that the power generation by the solar cells is working at 100% efficiency. However, at high angular velocities (above 100 rotation per minute), the MPPT cannot work, making the solar cells ineffective. Therefore, all of the incoming solar flux is absorbed by the satellite, slightly increasing the temperature of all components.

The mean value of the direction vector of the angular velocity tells the average lit surface area between the minimum (1) and the maximum ($\sqrt{3}$) of a perfect cube with unit length. It is calculated as follows:

$$\frac{16}{\pi^2} \int_0^{\pi/4} \int_0^{\pi/4} [\sin(\phi) + \cos(\phi)]\cos(\theta) + \sin(\theta)\mathrm{d}\phi\mathrm{d}\theta = 1.519, \tag{1}$$

where the ϕ angle is the axis of rotation which is normal to the top side of the cube. θ angle is its tilt from the Earth-Sun line. The problem is self-symmetrical by 90°, therefore, it is enough to calculate the integral from zero to 45° for both angles. 1.519 means 72° tilt angle which is used in the subsequent calculations. However, rotation at 1 rotation per minute is employed in the TN model, the average incoming heat was added in the FEM model as a boundary condition for the side panels to

Table 2
Thermal boundary conditions of the TN model.

Space temperature	2.7 K
Solar heat flux	1367 W/m^2
View factor of Earth	0.305
Avg. temperature of Earth	255 K
Avg. albedo	21%
Orbit height	550 km
Orbit period	5669 s
Lit/shadow ratio	64%/36%
Heat generation in the COM panel	203 mW
Heat generation inside the battery	10 mW
Efficiency of the solar cells	27%
Absorptance of the PCBs	0.85

avoid excessive run times.

Table 2 contains the key parameters of the thermal environment based on Refs. [21,22] and the satellite properties. The most power is dissipated by the communication and spectrum analyzer integrated circuit, located in the COM panel. It is followed by the battery, however, the heat generation drops as its internal resistance decreases with the increasing temperature which means a favorable self-controlling behavior. The radiation of Earth at 255 K falls in the infrared (IR) regime according to Wien's displacement law. Consequently, this radiation source cannot be used for energy generation since the solar cells absorb electromagnetic rays in the micrometer wavelength regime with very poor efficiency. Hence, all the incident IR radiation on the solar cells is converted into heat which was taken into account during boundary condition setup.

As for the other components, they maintain >95% efficiency, meaning few mW heat generation distributed among all the other panels. Therefore, this thermal power was neglected which brings one to the safe side. The concentrated thermal powers were considered as the average of the satellite operation during a full orbit. In the present case, Spectrolab Ultra Triple Junction Solar Cells are used. These are principally made for CubeSats, therefore, they were halved to fit the quarter-sized sides. After the breaking process, the full functionality was conserved with a slight asymmetry in the maximum output power. However, this cruel solution causes no problem since each side has a dedicated MPPT circuit. The size of the solar cells is ~1500 mm^2. The infrared radiation of Earth can be substituted by an equivalent heat flux to the satellite, see, e.g., [11]. Since it varies with the view factor, it is theoretically more correct to calculate the radiative heat transfer with Earth, like in Ref. [14] at 255 K average temperature [21].

The guaranteed operating temperature range of the used commercial electric components is at least $T = -40$ to $+80\,°C$. The Li-ion battery is the most sensitive to its operating temperature which is the bottleneck of the satellite, emphasized by other researchers as well [11,14]. It can withstand $T = -10$ to $+60\,°C$ during use and $T = 0$ to $+45\,°C$ while charging. In order to reduce the amplitude of temperature fluctuations, it is placed in the center of the frame with insulation. Note that using more than double-layer insulation has a negligible gain on the battery temperature since conduction becomes the governing heat transfer process via the connecting electric wires.

2.3. The TN model

In the thermal network model, all PCBs were assumed as a single node. Due to its limited operating temperature range, the battery is handled separately. Hence, the TN model consists of twelve nodes: six PCB sides, five inner PCBs, and the battery. The thermal characteristics of the threaded rods were split between the other components, considering their connection with the rods. The temperature variation was determined by Eq. (2) as the effect of convection is negligible in space:

$$c \cdot m \cdot \frac{dT}{dt} = \sum_{i=1}^{n} \dot{Q}_{rad} + \sum_{i=1}^{n} \dot{Q}_{cond} + \dot{Q}_{int}, \tag{2}$$

where t is the time, T is the temperature, $\dot{Q}$ is the thermal power, and *rad* and *cond* refer to radiation and conduction, respectively. $\dot{Q}_{int}$ notes the internal heat generation which is considered only in the battery and the COM panel. All the other electric components are highly efficient, and the panels showed negligible temperature difference during operation, verified by a thermal camera with 60 mK sensitivity per pixel. The absorptivity and emissivity of the surfaces were uniformly $\alpha = \varepsilon = 0.85$, as noted in Table 2. The view factors of the surfaces are calculated by the position of each panel without taking the effect of the mounted electric components into account. Thermal conduction was modeled between the OBC and the battery as the battery cap flanges are to be soldered to the back of the OBC panel. However, the battery is connected to the PCU with two wires which are responsible for the majority of the heat transfer. The third conduction contact group consists of the connected PCBs. All the thermal resistances used here were synchronized with those of the FEM simulation. Therefore, biased results are avoided, often caused by the human factor as there are some constants to tweak manually to get visually better results. Regarding boundary conditions, the two thermal models are strictly similar here. Nevertheless, the number of nodes of the FEM model is two magnitudes higher which leads to a more detailed solution, discussed in Section 3.

2.4. The FEM model

By applying a FEM model, there is an opportunity to obtain local results which depend upon the mesh size. It is essential to utilize a simplified geometry to reduce the mesh complexity which results in less number of equations to solve. Hence, the computational time decreases significantly, especially, when radiation is present which scales with T^4.

In order to simplify the geometry, the particular contacts between the PCBs, i.e., wires, bus connectors, were substituted by rectangles. The estimated thermal resistances were given between the contact and target surfaces. Furthermore, all the electronic parts were removed from the model, but their heat capacity was considered in their thermophysical properties. A mesh dependency analysis was performed first at three different face sizes, summarized in Table 3.

Time advancing was set to automatic with 10 s as initial and 50 s as maximum step sizes with duration of five full orbits. The effect of initial condition vanished after four orbits. Calculations by using the fine mesh resulted in <0.65 °C deviance in terms of minimum, maximum, and average temperatures of each part compared to the use of the mediocre mesh. For further simulations, the mediocre mesh was chosen as it reveals the temperature distribution better than the coarse mesh which resulted in ~1 °C deviance from the temperature field of the fine mesh.

Fig. 2 shows the mediocre mesh and the simplified internal structure with named parts. The size of the base plate is 58 x 64 mm which will be inserted into the rail of the launch pod. Besides the PCBs, the battery was included since it is more sensitive to the operating temperature than all the other electric components. The threaded rods were also considered since they establish a notable thermal bridge between the inner PCBs and the top and the bottom sides.

2.5. Additional boundary conditions of the FEM model

In the FEM model, the local domains were distinguished from each

Table 3
Settings of the mesh dependency analysis.

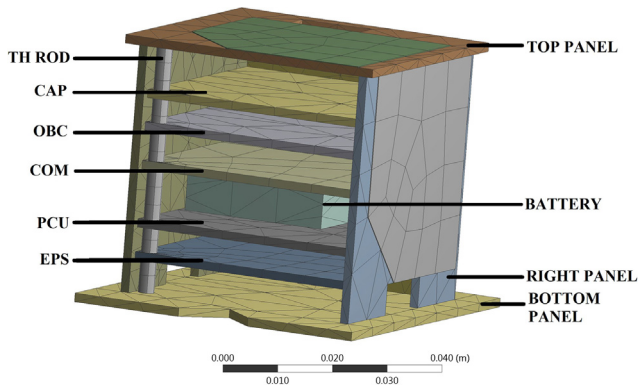| Mesh quality	Face size [mm]	# of nodes	# of elements
coarse	30	6606	2421
mediocre	10	9321	3008
fine	2	55780	15646

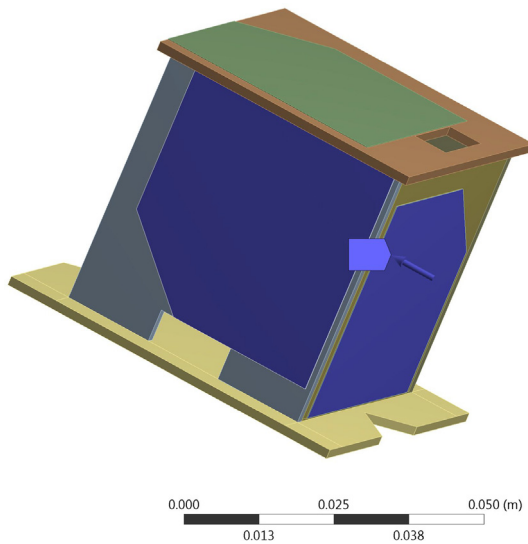**Fig. 2.** The FEM model with mediocre mesh and simplified geometry.

Fig. 3. Separately handled heat flux boundary condition on the middle side solar cells, highlighted in blue. (For interpretation of the references to color in this figure legend, the reader is referred to the web version of this article.)
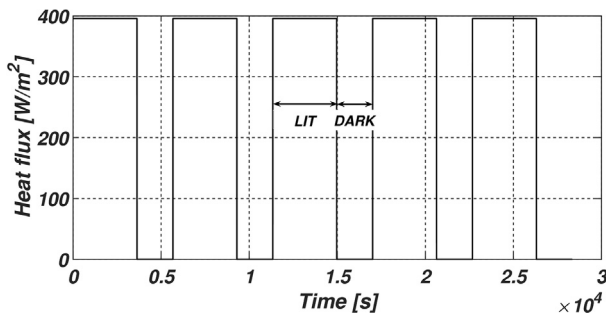

Fig. 4. Periodic heat flux boundary condition on the middle side solar cells, shown in Fig. 3.

Table 4
Thermal radiation boundary conditions in the FEM model.

Part	Heat flux source	Magnitude
Top panel	Incident solar	357 W/m^2
Top solar cell	Incident solar	282 W/m^2
Bottom panel	Albedo + IR	101 W/m^2
Bottom solar cell	Albedo + IR	74 W/m^2
Middle side panels	All three	473.8 W/m^2
Middle side solar cells	All three	395.7 W/m^2

other like the solar cell and the domain around it, shown in Fig. 3. Hence, by considering the heat flux boundary condition, its value locally varies even in one side since the solar cell transforms a portion of the incoming solar flux to electricity. Fig. 4 shows the square wave-like incident solar flux to a solar cell on orbit. The heat flux was averaged for each section to simplify the effect of rotation and significantly reduce the computational time. Table 4 summarizes all the averaged heat fluxes defined for the side panels of the satellite.

Ambient-to-surface type radiation was considered between the outer sides and space, summarized in Table 2. As for the inner surfaces, surface-to-surface radiation was defined. The view factors were automatically computed. Regarding other parameters and the solver, solely the default settings were used.

3. Results and discussion

As two different methods were applied to estimate the thermal balance of the SMOG-1 satellite, the present section starts with the TN due to its simplicity over the FEM model. Secondly, the results of the latter method are discussed in the light of the outcome of the former analysis. Note that the results are corresponding to a 550 km SSO, but a generalization of the findings was performed where it was reasonable.

3.1. TN results

The temperature variation of the battery is shown in Fig. 5 while Figs. 6 and 7 contain that of the side panels of the first five orbits, starting from a uniform +10 °C initial temperature. Since the solar flux varies by the orbit of the Earth around the Sun, minimum and maximum values correspond to 1322 and 1414 W/m^2, respectively.

The battery temperature violates the 0 to +45 °C regime, shown in Fig. 5. Nevertheless, the discharge conditions are met in the simulated case by the TN model. Therefore, charging should be intermittent as the battery temperature is expected to fall below 0 °C. The problem is that the low heat capacity results in a rapid heat loss in the shadow of Earth. Hence, when the satellite comes to light again, the battery temperature still falls due to the cooler panels. Based on the results at 1322 W/m^2 solar flux, only the second half of the orbit is suitable for storing the generated power by the solar cells. Therefore, an onboard logic must be implemented which detaches the battery from the power bus when the conditional minimum temperature is met. By assuming an estimated 203 mW average power consumption of the SMOG-1 and if only the half of the lit period can be used for storing power, the overall energy balance is still positive by a factor of at least 1.5. Consequently, the operation of the battery is safe from both thermal and energy point of views. This conclusion indicates that the battery technology set the current size limitation of the satellite which is able to operate continuously with full functionality in orbit.

The temperature variation of the top, the bottom, and a side panel is shown in Figs. 6 and 7 at the minimum and maximum solar flux,
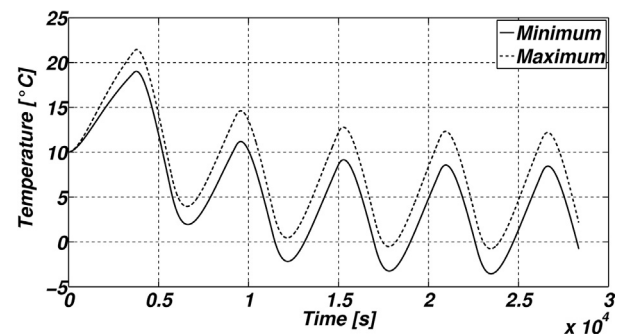

Fig. 5. Temperature variation of the battery during five orbits at minimum and maximum solar flux.
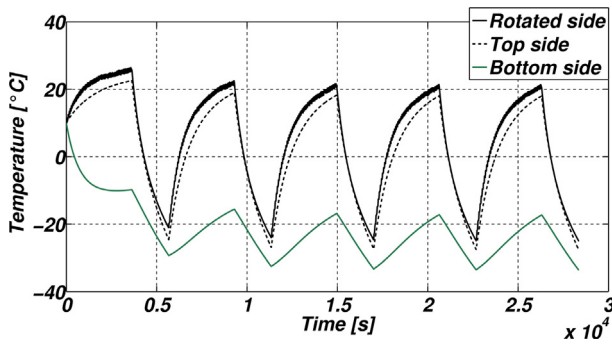
Fig. 6. Temperature variation of three sides during five orbits at 1322 W/m² solar flux.
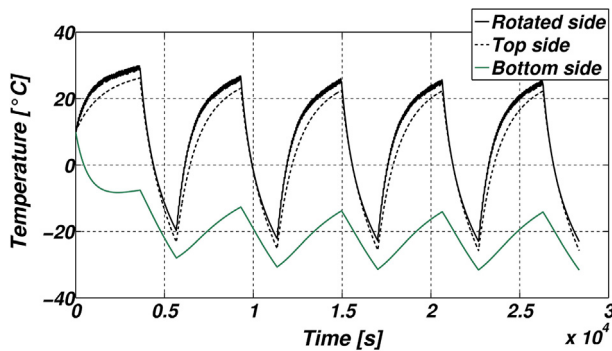

Fig. 7. Temperature variation of three sides during five orbits at 1414 W/m² solar flux.

respectively. The bottom side sees only the Earth, therefore, only the albedo and the infrared radiation increases its temperature which results in fluctuations between −14 °C and −34 °C. The side panel receives fluctuating solar flux due to its rotation which causes roughly 1 °C variation during a full turn at 1 rotation per minute. This PCB is characterized by the highest peak temperature of the satellite which is +25 °C.

Fig. 8 shows the characteristics of three inner PCBs which are not in connection with the battery in the same time frame as Fig. 6 at 1322 W/m² solar flux. CAP is subjected to the largest temperature fluctuations while EPS fluctuates with reduced amplitude and its temperature remains below of that of the other two PCBs. The temperature variation of the inner PCBs is closely in phase with the sides. Consequently, it can be stated based on the TN model that the electric components except the battery will operate within their allowed temperature range during the mission. However, the situation of the battery requires a more complicated programming and electrical layout, it fulfills all the requirements of safe and reliable operation.
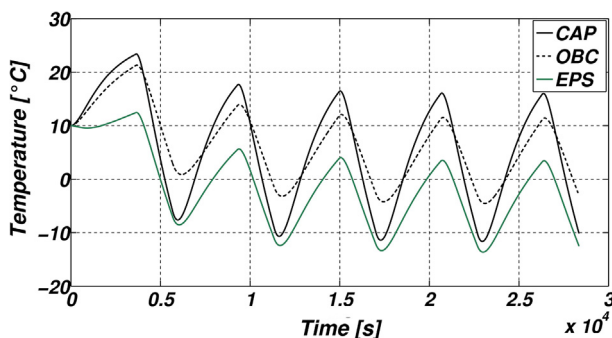

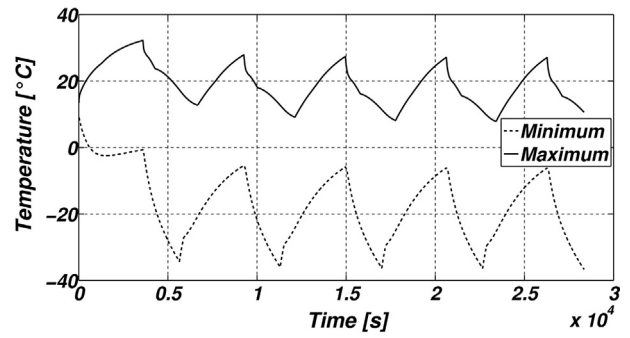**Fig. 8.** Temperature variation of three of the inner PCBs at 1322 W/m² solar flux.

Fig. 9. The global temperature history according to the FEM model at 1367 W/m² solar flux.

Based on the results of the TN model, it can be stated that the system is able to operate safely in the described thermal environment with a reasonable safety factor. Therefore, e.g., the loss of a single solar cell is expected not to harm the mission. Note that all these conditions are pessimistic since any penalty or damage to the power generation system results in more absorbed heat, hence, higher temperatures. Consequently, the increasing battery temperature leads to wider charging regimes.

3.2. FEM results

In the previous section, it was shown that there is no significant difference between the temperature values in the case of minimum and maximum solar fluxes. Therefore, the present analysis proceeds with the time-averaged solar flux applied, i.e., 1367 W/m².

Fig. 9 shows the global temperature extremes over time, and Fig. 10 shows the global temperature distribution after six hours (roughly three and a half orbit) simulation time. It corresponds to the quasi-steady behavior; the transient effects due to the initial conditions already vanished. Note that there is a global temperature peak at this time instant. According to the simulations, a stable periodic temperature oscillation appears by orbiting as it was also concluded by Gaite et al. [23,24]. In the followings, the results of the FEM and TN models will be presented and discussed.

Among the electronic parts, the battery has a critical role as it was emphasized earlier; its temperature variation is shown in Fig. 11. The internal thermal resistance of the battery can be neglected since there is no significant temperature difference within its physical structure. Consequently, modeling a battery with a single node might be a reasonable simplification for small-scale satellites. Comparing the results
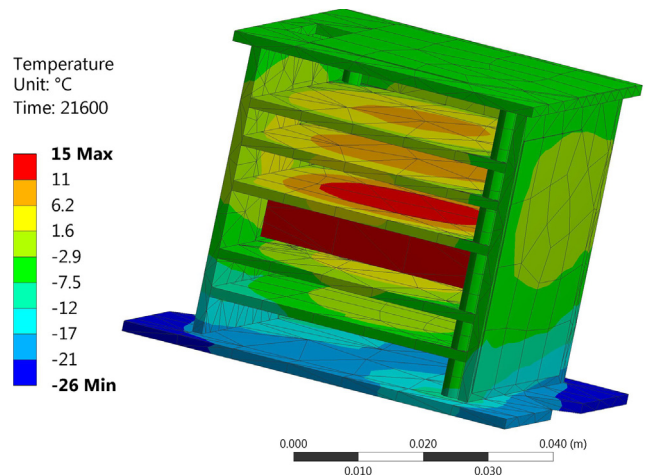

Fig. 10. The global temperature distribution after six hours simulation time at 1367 W/m² solar flux.
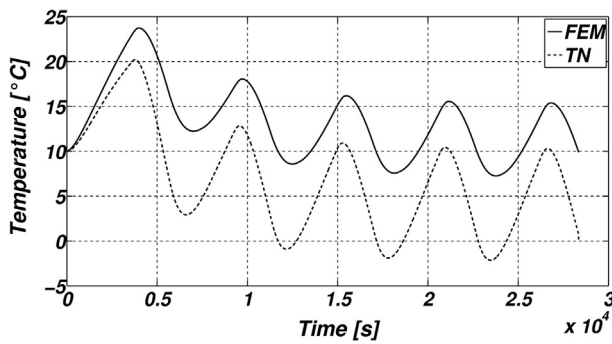
Fig. 11. The battery temperature history at 1367 W/m² solar flux.

Fig. 13. The bottom side temperature history at 1367 W/m² solar flux.

Fig. 14. The front side temperature history at 1367 W/m² solar flux.

to the TN model, the FEM predicts higher temperatures under the same boundary conditions which confirm the safe operation, including the stricter conditions of charging the battery. Furthermore, a noticeable phase lag appears between these time histories. It is originated from the simplicity of TN model; the overall thermal resistances are smaller due to the one PCB – one node simplification.

Regarding the sides of the cube, there are three characteristically distinguishable parts. The first is the top side, which receives only the solar flux, shown in Fig. 12. Fig. 13 presents the bottom side which is affected by the albedo and the infrared radiation of Earth. The third one discussed here is the front side which is thermally the same as the remaining three sides. Fig. 14 shows the temperature history of this face, influenced by all radiative effects. Paying attention again to the phase lag between the FEM solution and the TN model, shown in Fig. 13, it appears in the opposite direction compared to the battery temperature history of Fig. 11. However, this lag disappears in case of the rotating sides in Fig. 14.

The spatial temperature distribution of the inner surface of the sides after six hours simulation time is shown in Figs. 15–17, calculated by the FEM model. The blue regime in the middle of Fig. 15 shows that the inner PCBs, hence, the CAP, are cooler and draw heat from the top panel via radiation. The outer regions are characterized by higher temperature since the side panels are warmer. This phenomenon peaks below the slot which allows wire data connection and battery charging. It also hosts the Remove before flight pin which switches off the system while inserted.

Since the bottom panel, shown in Fig. 16, receives mostly the IR radiation of Earth in addition to albedo, it is cooler than the top panel. Here, the thermal bridge effect of the threaded rods is clearly visible. This can also be found on the top side, however, its magnitude almost fades since that side is warmer.

Fig. 17 shows the temperature distribution of a side panel. The horizontal asymmetry is due to the diagonally placed threaded rods which transport heat to the cooler parts. Since the side panels receive the most heat flux, shown previously in Table 4, the central region is characterized by higher temperatures. Note that the global minimum
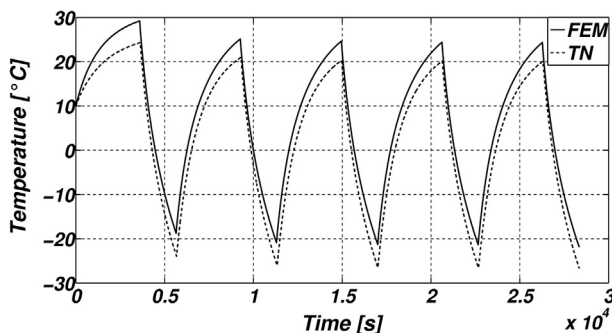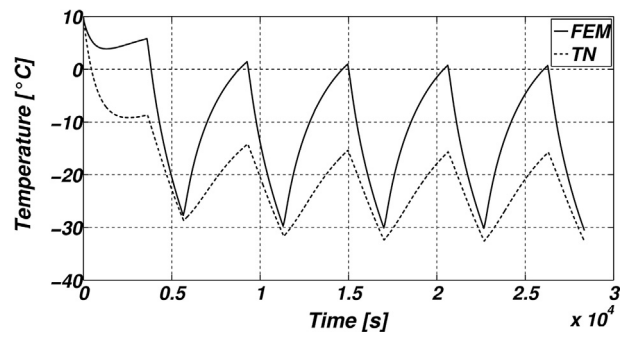

Fig. 15. Spatial temperature distribution of the top side at 1367 W/m² solar flux.

and maximum temperatures at 21,600 s simulation time were 15 and −26°, respectively. The temperature extremes at this time instant were located on the outer surface of the sides.

As for the summary of the comparison of the two methods, it can be stated that the FEM model estimates generally higher temperatures. Since the temperature of a PCB in the case of the TN model is concentrated at a single point, it leads to increased heat losses through radiation to the ambient as it scales with the fourth power of the absolute temperature. However, the TN model was created in MATLAB® Simulink® environment, it contains no special functions which allow the construction of similar solvers in any open source environment. Moreover, a single run takes ~10 s while the FEM setup at mediocre mesh requires 30 min on a PC, being another advantage of the TN model. The underprediction of the temperature compared to measurements is shown by [17]. Note that advanced numerical approaches like genetic algorithm [15], differential evolution, or other metaheuristic
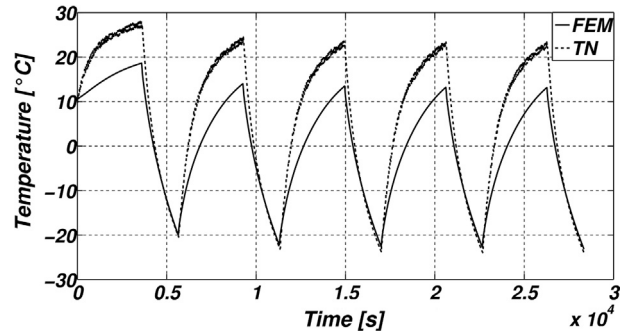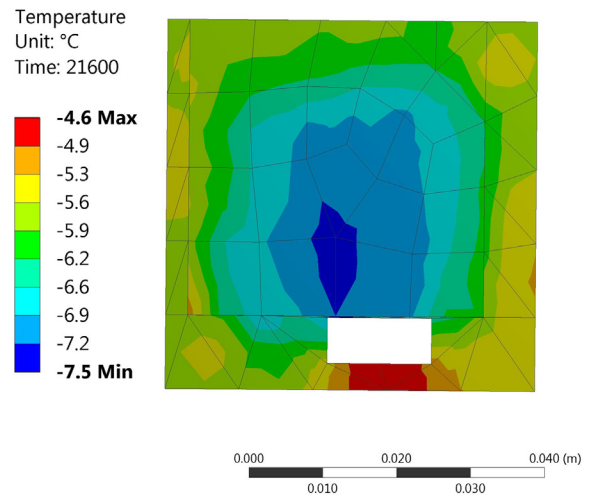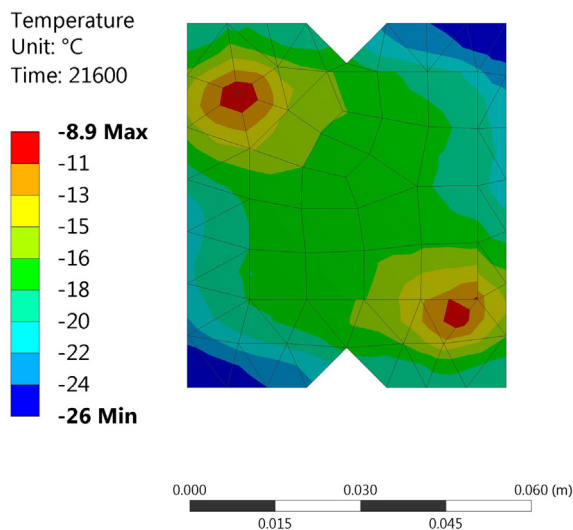

Fig. 12. The top side temperature history at 1367 W/m² solar flux.

Fig. 16. Spatial temperature distribution of the bottom side at 1367 W/m^2 solar flux.
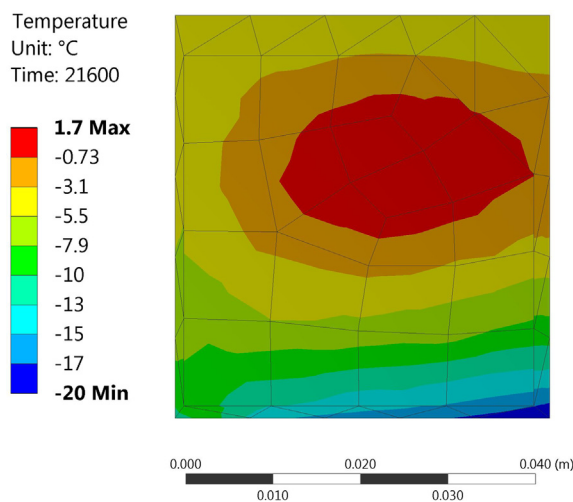

Fig. 17. Spatial temperature distribution of the front side at 1367 W/m^2 solar flux.

methods require reliable measurement data which are often not available in the conceptual design phase.

If one wishes to further improve the accuracy of a TN model in a radiation-dominated environment like space, the number of divisions should be increased which provides similar results to that of a FEM simulation [11]. If both methods are available at will, then a wise introduction of virtual thermal resistances can be performed to get an accurate but less computation-intensive TN model. It was concluded that even a tiny satellite is thermally safe in the vicinity of Earth. Bulut and Sozbir [4] have shown that the equilibrium temperature of the satellite is expected to decrease by a small extent up to a 2000 km orbit. Therefore, the results of the present paper might be used at other low-Earth orbit profiles as well.

4. Conclusions

Thermal analysis of the SMOG-1 PocketQube (or picosatellite) was presented by comparing the results of the thermal network (TN) and finite element methods (FEM). This investigation assumed a 550 km Sun Synchronous Orbit at 98° inclination, but the methods shown here are generally applicable to similar problems. Based on the results, the following conclusions were derived:

- The FEM model predicts higher temperatures than the one panel-one node TN model. The reason behind this is that the outer panels consisting of numerous nodes which allow lower temperature losses due to radiation as the thermal resistance between them is considered, unlike in the TN model. As a side effect, the FEM model requires significantly more time to solve (30 min against 10 s in the present case).

- Despite the simplicity of the TN model regarding the concentrated thermal capacities and resistances, it is adequate for temperature prediction over extended time and real-time analysis. Compared to the FEM model, the deviations are explained by the different mathematical approaches and the number of nodes.

- Even though the small-sized PocketQube satellites have very low overall heat capacity, they can perform continuous operation since a Li-ion battery can be kept within its operating temperature range at a low-Earth orbit. Nevertheless, the more conservative TN model predicted at a minimum solar flux of 1322 W/m^2 that its temperature might fall below 0 °C when discharge is unrestricted, but charging is not advised. However, the reduced time for charging still allows a continuous operation since 1.5 times the energy demand of a single orbit can be stored during the restricted time frame.

Acknowledgments

Appendix A. Supplementary material

Supplementary data associated with this article can be found, in the online version, at http://dx.doi.org/10.1016/j.applthermaleng.2018.05.020.

References

[1] S. Lee, A. Hutputanasin, A. Toorian, W. Lan, R. Munakata, J. Carnahan, D. Pignatelli, A. Mehrparvar, CubeSat Design Specification. rev 13, 2014.

[2] J. Bouwmeester, J. Guo, Survey of worldwide pico- and nanosatellite missions, distributions and subsystem technology, Acta Astronaut. 67 (7-8) (2010) 854–862, http://dx.doi.org/10.1016/j.actaastro.2010.06.004.

[3] R. Shimmin, Small Spacecraft Technology State of the Art (NASA/TP2015216648/REV1), Tech. rep., NASA, Mission Design Division Ames Research Center, Moffett Field, California, 2016. < https://www.nasa.gov/centers/ames/engineering/state-of-the-art > .

[4] M. Bulut, N. Sozbir, Analytical investigation of a nanosatellite panel surface temperatures for different altitudes and panel combinations, Appl. Therm. Eng. 75 (2015) 1076–1083, http://dx.doi.org/10.1016/j.applthermaleng.2014.10.059.

[5] S. Speretta, T. Pérez Soriano, J. Bouwmeester, J. Carvajal Godínez, A. Menicucci, T. G. Watts, P.P. Sundaramoorthy, J. Guo, E.K.A. Gill, Cubesats to pocketqubes: opportunities and challenges, in: Proceedings of the 67th International Astronautical Congress (IAC), IAF, 2017, pp. 1–5.

[6] L. Dudás, L. Szűcs, A. Gschwindt, The spectrum monitoring system by Smog-1 satellite, Conference on Microwave Techniques (COMITE), 2015, IEEE, 2015, pp. 1–4, , http://dx.doi.org/10.1109/COMITE.2015.7120316.

[7] L. Dudás, A. Gschwindt, The communication and spectrum monitoring system of Smog-1 PocketQube class satellite, 21st International Conference on Microwave, Radar and Wireless Communications (MIKON), 2016, IEEE, 2016, pp. 1–4, , http://dx.doi.org/10.1109/MIKON.2016.7491999.

[8] B.D. Olaszi, V. Józsa, J. Ladányi, Energy management of a PocketQube satellite, 5th International Youth Conference on Energy (IYCE), 2015, IEEE, 2015, pp. 1–5.

[9] G. Géczy, Results from SMOG-1 PocketQube, in: PocketQube Workshop, Delft, 2017, pp. 31.

[10] A. Scholz, J.N. Juang, Toward open source CubeSat design, Acta Astronaut. 115 (2015) 384–392, http://dx.doi.org/10.1016/j.actaastro.2015.06.005.

[11] S. Corpino, M. Caldera, F. Nichele, M. Masoero, N. Viola, Thermal design and analysis of a nanosatellite in low earth orbit, Acta Astronaut. 115 (2015) 247–261, http://dx.doi.org/10.1016/j.actaastro.2015.05.012.

[12] A. Torres, D. Mishkinis, T. Kaya, Mathematical modeling of a new satellite thermal architecture system connecting the east and west radiator panels and flight performance prediction, Appl. Therm. Eng. 65 (1-2) (2014) 623–632, http://dx.doi.org/10.1016/j.applthermaleng.2013.11.040.

[13] P. Fortescue, G. Swinerd, J.P.W. Stark (Eds.), Spacecraft Systems Engineering, fourth ed., Wiley Online Library, 2003, , http://dx.doi.org/10.1002/9781119971009.ch2.

[14] N.D. Anh, N.N. Hieu, P.N. Chung, N.T. Anh, Thermal radiation analysis for small satellites with single-node model using techniques of equivalent linearization, Appl. Therm. Eng. 94 (2016) 607–614, http://dx.doi.org/10.1016/j.applthermaleng.2015.10.139.

[15] E. Escobar, M. Diaz, J.C. Zagal, Evolutionary design of a satellite thermal control system: real experiments for a CubeSat mission, Appl. Therm. Eng. 105 (2016) 490–500, http://dx.doi.org/10.1016/j.applthermaleng.2016.03.024.

[16] J. Rotteveel, A. Bonnema, Thermal control issues for nano- and picosatellites, in: 57th International Astronautical Congress, International Astronautical Congress, International Astronautical Federation, 2006, pp. 1–8. http://dx.doi.org/10.2514/6.IAC-06-B5.6.07.

[17] J.-R. Tsai, Overview of satellite thermal analytical model, J. Spacecraft Rockets 41 (1) (2004) 120–125, http://dx.doi.org/10.2514/1.9273.

[18] M.F. Diaz-Aguado, J. Greenbaum, W.T. Fowler, E.G. Lightsey, Small satellite

[19] thermal design, test and analysis, in: Proceedings of the SPIE, 2006, pp. 12. http://dx.doi.org/10.1117/12.666177.

[19] C.-J. Fong, A. Lin, A. Shie, M. Yeh, W.-C. Chiou, M.-H. Tsai, P.-Y. Ho, C.-W. Liu, M.-S. Chang, H.-P. Pan, S. Tsai, C. Hsiao, Lessons learned of NSPOs picosatellite mission: YamSat-1A, 1B & 1C, in: Proceedings of the 16th Annual AIAA/USU Conference on Small Satellites, SSC02-X-6, 2002, pp. 12. < http://digitalcommons.usu.edu/smallsat/2002/all2002/60/ > .

[20] D. Barnhart, M.N. Sweeting, Right-sizing small satellites, in: Proceedings of the 28th Annual AIAA/USU Conference on Small Satellites, 2014, 2014, pp. 1–8.

[21] D.G. Gilmore, Spacecraft thermal control handbook. Vol. 1. Fundamental Technologies, El Segundo, California, Aerospace Press, 2002. http://dx.doi.org/10.2514/4.989117.

[22] J.H. Henninger, Solar Absorptance and Thermal Emittance of Some Common Spacecraft Thermal-Control Coatings (No. NASA-RP240400-1121), Tech. rep., National Aeronautics and Space Administration, Goddard Space Flight Center, Greenbelt, Maryland, 1984.

[23] J. Gaite, A. Sanz-Andrés, I. Pérez-Grande, Nonlinear analysis of a simple model of temperature evolution in a satellite, Nonlinear Dyn. 58 (1) (2009) 405, http://dx.doi.org/10.1007/s11071-009-9488-x.

[24] J. Gaite, Nonlinear analysis of spacecraft thermal models, Nonlinear Dyn. 65 (3) (2011) 283–300, http://dx.doi.org/10.1007/s11071-010-9890-4.